Supporting Information

Tort *et al.* 10.1073/pnas.0810524105

SI Text

Training and Data Acquisition. Behavioral training and electrophysiology recording methods were approved by the Committee on Animal Care of Massachusetts Institute of Technology and are described in detail by DeCoteau *et al.* (1, 2). Briefly, 6 male Sprague–Dawley rats were implanted with head stages containing 12 tetrodes, with 6 tetrodes targeting the dorsomedial caudoputamen (AP: +1.7 mm, ML: 1.8 mm, DV: 3.6–4.6 mm) and 6 tetrodes targeting the CA1 region of the dorsal hippocampus (AP: −3.3 mm, ML: 2.2 mm, DV: 2.4–2.8 mm). Tetrodes were lowered to their target depths during a 1-week postsurgical recovery period. Rats then received daily training sessions (usually 40 trials) on an auditory tone-cued T-maze task. Rats were trained to turn right or left at the choice point of the maze as instructed by 1- and 8-kHz tone cues. A click warning cue preceded the opening of a start gate. Rats were rewarded with chocolate sprinkles if the baited goal was correctly approached. Throughout training, LFPs were amplified (gain: 1,000), filtered (1–475 Hz) and continuously sampled at 1 kHz by using a Cheetah recording system (Neuralynx). An anchor screw in the rat's skull or the external ground of the recording system was used as reference. In some sessions, a striatal tetrode was used as reference to verify local generation of striatal field potentials. Tetrode tracks and microlesions marking the final tetrode position were identified in 24-μm-thick sections of formalin-fixed tissue stained for Nissl substance. In the hippocampus, the definition of "deep" and "superficial" CA1 layers was performed based on the phase reversal of the theta wave combined with daily records of tetrode depth.

Data Analysis. All analyses were done by using MATLAB 7.5 software by MathWorks. Computations were carried out on an Intel Pentium III Linux Cluster at Boston University (http://scv.bu.edu/computation/linuxcluster/). Unless otherwise specified, the analyses were performed on 1,000-ms windows centered at the task events.

The modulation index and the phase-to-amplitude comodulograms. To quantify the amplitude modulation by phase, we created a modulation index (MI) based on a normalized entropy measure previously described in Hurtado *et al.* (3). This index is able to detect cross-frequency coupling between 2 frequency ranges of interest. We denote the amplitude and the phase frequency ranges under analysis by f_A and f_p, respectively. We denote as $x_{\text{raw}}(t)$ the raw signal (i.e., the unfiltered LFP; Fig. S2*a*). The MI is calculated as described below (see Fig. S2).

1. First, $x_{\text{raw}}(t)$ is filtered at the 2 frequency ranges under analysis (f_p and f_A). We denote the filtered signals as $x_{fp}(t)$ and $x_{fA}(t)$ (Fig. S2 *b* and *c*).
2. The time series of the phases of $x_{fp}(t)$ [denoted as $\phi_{fp}(t)$] is obtained from the standard Hilbert transform of $x_{fp}(t)$ (Fig. S2*d*). The Hilbert transform is also applied to $x_{fA}(t)$ to extract the time series of the amplitude envelope of $x_{fA}(t)$ [denoted as $A_{fA}(t)$; (Fig. S2*e*)]. The composite time series $[\phi_{fp}(t),A_{fA}(t)]$ is then constructed, which informs the amplitude of the f_A oscillation at each phase of the f_p rhythm (Fig. S2*f*).
3. Next, the phases $\phi_{fp}(t)$ are binned into eighteen 20° intervals (0° to 360°), and the mean of A_{fA} over each phase bin is calculated (Fig. S2*g*). We denote as $\langle A_{fA}\rangle_{\phi_{fp}}(j)$ the mean A_{fA} value at the phase bin j.
4. We then apply the entropy measure H, defined by:

$$H = -\sum_{j=1}^{N} p_j \log p_j,$$

where $N = 18$ (i.e., the number of bins) and p_j is given by

$$p_j = \frac{< A_{f_A} >_{\phi_{f_p}}(j)}{\sum_{j=1}^{N} < A_{f_A} >_{\phi_{f_p}}(j)}.$$

5. The MI is finally obtained by normalizing H by the maximum possible entropy value ($H_{\max}$), which is obtained for the uniform distribution $p_j = 1/N$ (and hence $H_{\max} = \log N$):

$$MI = \frac{H_{\max} - H}{H_{\max}}.$$

A MI value of 0 indicates lack of phase-to-amplitude modulation (i.e., constant $\langle A_{fA}\rangle_{\phi_{fp}}$ for all phase bins), and larger MI values result from stronger phase-to-amplitude modulation.

The comodulogram plot is obtained by representing in pseudocolor scale the MI values of multiple (f_p,f_A) pairs, with f_p calculated in 1-Hz steps with 2-Hz bandwidths and f_A in 2-Hz steps with 4-Hz bandwidths (Fig. S2*i*). We note however that the comodulogram plots reported in the figures of the main article were further subjected to statistical analysis (described below), and the value of each (f_p,f_A) entry was obtained by $MI_{\text{stat}} = MI - MI_{\text{thresh}}$, where MI_{thresh} is the significance threshold. Any value >0 in the comodulogram plots shown in the main article is statistically significant.

The MI statistical analysis. To assess the statistical significance of the MI values, we worked with a distribution of 200 surrogate MI values achieved by applying the MI measure to trial shuffled composite time series $[\phi_{fp}(t),A_{fA}(t)]$. To create the trial shuffled composite time series, $\phi_{fp}(t)$ is calculated from trial m, and $A_{fA}(t)$ is calculated from trial n, with m and n randomly chosen from $[1.,K]$, K denoting the total number of trials (usually $K = 40$ in each session). Assuming a normal distribution of the surrogate MI values, a significance threshold (MI_{thresh}) is then calculated by using $P < 0.01$.

Remark: Canolty *et al.* (4) used a modulation index that is computed based on the mean vector of a complex time series defined by $A_{fA}(t)e^{i\phi_{fp}(t)}$ compared with a distribution of surrogate means created by offsetting $A_{fA}(t)$ and $\phi_{fp}(t)$ by some large time lag τ (i.e., a surrogate vector is defined by $A_{fA}(t + \tau)e^{i\phi_{fp}(t)}$; see supporting information of ref. 4). We worked with the modulation index described above instead of their measure because large time records are required to create the surrogate data necessary to compute the Canolty *et al.* index; we did not have such long records (each trial lasts a few seconds, and the task events were analyzed in 1,000-ms windows). Nevertheless, we observed the same qualitative results when working with a variant of Canolty *et al.* index, which was obtained by using the shuffled trial procedure to create the surrogate data (data not shown). However, we again chose to work with our modulation index instead of this variant because our index is potentially able to detect bimodal distributions of phase of maximal amplitude that would not be seen by the mean vector analysis (e.g., if the gamma amplitude of a given signal is modulated by the theta

phases of ϕ and of $\phi + \pi$, then the amplitude peaks would cancel the other in the mean vector analysis).

Theta trough time-locked plots. The time–frequency plots of the mean normalized power time-locked to the theta trough were computed as described in Canolty *et al.* (4). Briefly, the theta troughs are identified by finding the local minima of the phase time series (obtained by applying the Hilbert transform to the theta-filtered signal). A set of normalized instantaneous power series is calculated as follows: first the raw signal $x_{raw}(t)$ is filtered into several bands with center frequencies from 10 to 400 Hz, in 2-Hz steps with 4-Hz bandwidths; next, each band-pass-filtered signal is normalized by subtracting the temporal mean and dividing by the temporal standard deviation; last, the amplitude envelope is calculated for each normalized signal (by using the Hilbert transform) and subsequently squared element-wise. The time–frequency plot is generated by averaging 800-ms epochs extracted from the normalized instantaneous power centered at the theta troughs (producing what was defined as the mean normalized power time-locked to the theta trough). The theta trough time-locked plots were computed by using LFP data between the "Start" and "Turn-End" task events.

Averaged raw signals centered at the fast oscillations peaks. The results shown in Figs. 3*B* and 4 *B* and *C* and Fig. S4*b* were obtained as follows: first the signal was filtered at the fast oscillation frequency range under study (e.g., 80–120 Hz, HG or HFO). Then, a time series indicating the times of the peaks of the filtered signal was constructed, with the requirement that the peak times are separated by at least 100 ms from each other (i.e., just the highest peaks within 100-ms windows were used; the requirement of 100 ms is to avoid selecting multiple peaks within a theta cycle). The final trace is then obtained by averaging 600-ms epochs of the raw signal centered at the time points corresponding to the fast oscillation peaks. Note that if the fast oscillation peaks occur more often in a given theta phase (e.g., at the trough of the oscillation), one expects to be able to observe both the fast oscillation and the theta wave in the averaged raw signal, because the theta waves are time-locked to the peak times. On the other hand, if the fast oscillation possesses no amplitude modulation by the theta phase, the theta waves will be out of phase among the several epochs and will be averaged out from the final mean LFP trace. In applying this measure, no assumptions regarding the phase frequency of the cross-frequency coupling are made; just the frequency band under study for amplitude modulation is required as input data. However, by also filtering the signal at the theta band and extracting the time series of the theta phases, one can assess the phases where the fast oscillation peaks occurred. A histogram showing the number of peaks in each theta phase can then be constructed and used as another tool to assess phase-to-amplitude coupling. Such histograms are reported together with the averaged LFP traces in the figures. The averaged raw signals centered at the fast oscillation peaks and the corresponding histograms were computed by using LFP data between the Start and Turn-End task events.

Multiple regression analyses. Multiple regression analysis was performed by using MATLAB *regress.m* function. The regression analysis was used to study relations between the cross-frequency couplings and the power of the rhythms. More specifically, we studied the relations between power and the MI values obtained for the fast oscillations amplitude and the theta phase. In Figs. S6–S9, the intensity of the cross-frequency coupling, or "modulation," was assessed by the $\langle MI \rangle_\theta$ value. The symbol $\langle MI \rangle_\theta$ denotes the mean MI values calculated over a rectangular area of the comodulogram plot defined by the intersection of theta range (in the phase axis) and the fast oscillation range under study (in the amplitude axis). For example, HFO $\langle MI \rangle_\theta$ is obtained by calculating the mean over the (f_p, f_A) entries pertaining to the rectangle (7, 12)Hz × (120, 180)Hz. Similarly, LG $\langle MI \rangle_\theta$ is calculated over (7, 12)Hz × (30, 60)Hz, and HG $\langle MI \rangle_\theta$ is the mean over (7, 12)Hz × (60, 100)Hz. Lastly, 80–120 Hz $\langle MI \rangle_\theta$ denotes the *MI* mean over (5, 9)Hz × (80, 120)Hz as the amplitude modulation occurred in a lower theta range in the striatum. We note that we chose to work with the mean over the comodulogram entries ($\langle MI \rangle_\theta$) as opposed to computing the MI for wide-band-filtered signals because the latter analysis may be affected by the 1/*f* power distribution. For example, take the case in which the amplitude of 85–95 Hz is modulated by the theta phase. This narrow band modulation might not be evident when one calculates the MI for the signal wide-band filtered at the HG range (60–100 Hz). This is because the amplitude envelope of the HG-filtered signal is mainly due to the frequencies near 60 Hz (by 1/*f*, the lower the frequency, the higher the amplitude), which present no modulation by the theta phase in this example.

The mean modulation index values ($\langle MI \rangle_\theta$) were subjected to regression analyses against the power of the distinct rhythms. Before this procedure, however, the $\langle MI \rangle_\theta$ value in each task event was expressed as the ratio to the pre-trial value, and the power values were expressed as *z*-scores. This normalization was performed to allow the combined analysis of distinct electrodes and animals.

Cross-structure cross-frequency coupling analysis. The comodulograms generated during the cross-structure coupling analysis were obtained by following the same steps as described above for the analysis within each structure. However, the phase time series ϕ_{fp} and the amplitude time series A_{fA} were each obtained from a different region, as labeled in Fig. 5*A*. We note that there are 2 ways in which the phase of a low-frequency oscillation in structure *X* (defined as X_f) could modulate the amplitude of a high-frequency oscillation in structure *Y* (defined as Y_{fA}). The first consists of cross-frequency coupling within structure *Y* (i.e., $Y_{fp} \rightarrow Y_{fA}$) combined with high phase coherence at low frequencies between *Y* and *X*. The result is an indirect coupling between structures: $X_{fp} \rightsquigarrow Y_{fA}$; because the (low frequency) phase in *Y* and (low frequency) phase in *X* are strongly coherent, the phase in *X* appears to modulate the (high frequency) amplitude of *Y*. The second consists of direct cross-frequency coupling between structures: $X_{fp} \rightarrow Y_{fA}$. In this case, the (low frequency) phase of *X* modulates the (high frequency) amplitude of *Y*, irrespective of the (low frequency) phase coherence levels between *X* and *Y*. The presence of strong phase coherence between *X* and *Y*, as observed in this study between the hippocampus and the striatum, does not by itself invalidate the possibility of a direct interaction between X_{fp} and Y_{fA}.

Speed-controlled analyses. The same animal was used in Fig. S8 *A–C*, and the means were taken over several experimental sessions ($n = 13$). The group results (over rats, electrodes, and experimental sessions) shown in Fig. S8*D* were obtained during the Tone Onset event. Within each experimental session, the trials were divided into 4 groups according to the rat's speed [i.e., divided into 4 speed quartiles (IQ)]. The mean MI values ($\langle MI \rangle_\theta$, see session above) were then computed for each IQ group. The LG, HG, and HFO $\langle MI \rangle_\theta$ values were computed over the hippocampal electrodes, and the 80- to 120-Hz $\langle MI \rangle_\theta$ over the striatal electrodes. Each IQ group within an experimental session included ≈10 trials (i.e., sessions typically consisted of 40 trials). To allow the combined analyses of distinct animals, electrodes, and sessions, the $\langle MI \rangle_\theta$ values were normalized by dividing each IQ $\langle MI \rangle_\theta$ value by the mean over the quartiles.

Filter settings. All filtering used for the data analysis was done by using a linear finite impulse response (FIR) filter by means of *eegfilt()* function from the EEGLAB toolbox (5), which is available for free download at http://sccn.ucsd.edu/eeglab/. The filter order depends on the low-frequency cutoff, and it is given by 3 times the ratio of the sampling frequency to the low-frequency cutoff (rounded to the nearest integer toward zero). The *eegfilt()* function calls the Matlab routine *filtfilt()*, which applies the filter forward and then again backward, to ensure that

phase delays introduced by the filter are nullified. Nevertheless, we note that the absolute phase in our and other studies should be interpreted with caution, because recent evidence has been suggesting the existence of phase distortions secondary to particular characteristics of electrodes (6).

As mentioned in *Training and Data Acquisition*, above, all of the LFP data analyzed in Matlab had been previously band-pass filtered between 1 and 475 Hz by using the Cheetah recording system. We note that this procedure could be causing an artificial 3-Hz peak seen in the striatal power spectra during the first task events (Fig. 1*C*), which would otherwise look like a typical 1/*f* curve. This band-pass filtering, however, does not influence the spectral peaks at higher theta frequencies seen in the striatum during the middle of the task (e.g., during the Tone Onset event). We also observe that the maximum active frequency in the HFO band detected in our study could be influenced by low-pass filtering at 475 Hz. However, we do not believe this is a major concern because (*i*) several of our comodulograms showed modulated HFO with a limited frequency range, which were considerably below 475 Hz, and (*ii*) our analyses (more specifically, the comodulograms and the time–frequency plots locked to the theta trough) are normalized to the power of the oscillation; it is known that, whereas filtering considerable attenuates the amplitude of an oscillation, it does not completely remove it from the signal.

Remark: We were unable to analyze the relationship between the spikes and the LFPs recorded on the tetrodes due to incomplete spike datasets for enough tetrodes for sufficient numbers of simultaneous recordings. Such studies will be critical for understanding how the activities of single neurons and of neural ensembles are related to the cross-frequency couplings described here.

1. DeCoteau WE, *et al.* (2007) Learning-related coordination of striatal and hippocampal theta rhythms during acquisition of a procedural maze task. *Proc Natl Acad Sci USA* 104:5644–5649.
2. DeCoteau WE, *et al.* (2007) Oscillations of local field potentials in the rat dorsal striatum during spontaneous and instructed behaviors. *J Neurophysiol* 97:3800–3805.
3. Hurtado JM, Rubchinsky LL, Sigvardt KA (2004) Statistical method for detection of phase-locking episodes in neural oscillations. *J Neurophysiol* 91:1883–1898.
4. Canolty RT, *et al.* (2006) High gamma power is phase-locked to theta oscillations in human neocortex. *Science* 313:1626–1628.
5. Delorme A, Makeig S (2004) EEGLAB: An open source toolbox for analysis of single-trial EEG dynamics including independent component analysis. *J Neurosci Methods* 134:9–21.
6. Nelson MJ, Pouget P, Nilsen EA, Patten CD, Schall JD (2008) Review of signal distortion through metal microelectrode recording circuits and filters. *J Neurosci Methods* 169:141–157.

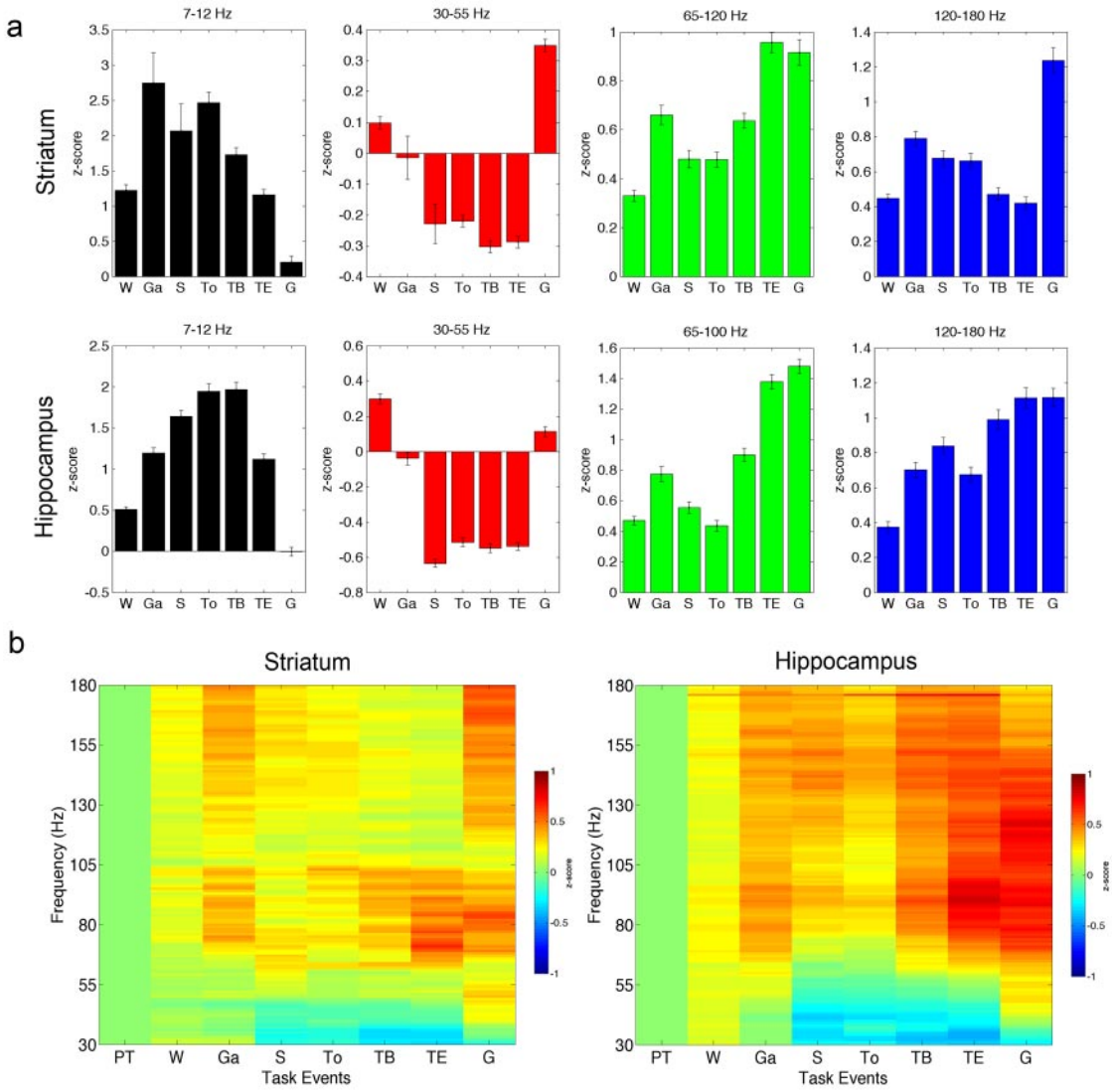

Fig. S1. Distinct frequency bands exhibit different power variations during the T-maze task. (*a*) Changes in the striatal (*Upper*) and hippocampal (*Lower*) oscillations power during distinct task events. Results are reported as the *z*-score of the average power with respect to the pre-trial average power in each frequency band. We show the average over all tetrodes, sessions, and animals (striat $n = 303$; hipp $n = 360$). Similar power variations were found in both the striatum and in the hippocampus: theta power (black bars) increases during the task, peaking at the middle of the maze, and decays to pre-trial values when the goal is approached. Low gamma power (LG, red bars) diminishes during the middle of the task, whereas high gamma (HG, green bars) and high-frequency oscillations (HFO, blue bars) powers tend to increase throughout the task events (notice, however, the difference in definition of high gamma in the striatum, in accordance with the results presented in Figs. 1 and 3 in the main article). Qualitatively similar results were found when each rat was analyzed individually. Error bars represent SEM. (*b*) Event-frequency power decomposition of striatal (*Left*) and hippocampal (*Right*) LFPs. Pseudocolor scale represents *z*-score with respect to the pre-trial period averaged over all tetrodes, sessions, and animals. Note that although the HG and HFO bands seem to be indistinguishable in the hippocampus, other analyses performed in this work revealed that they are distinct physiological processes. Events labels: PT, pre-trial; W, warning; Ga, gate; S, start; To, tone onset; TB, turn begin; TE, turn end; G, goal.

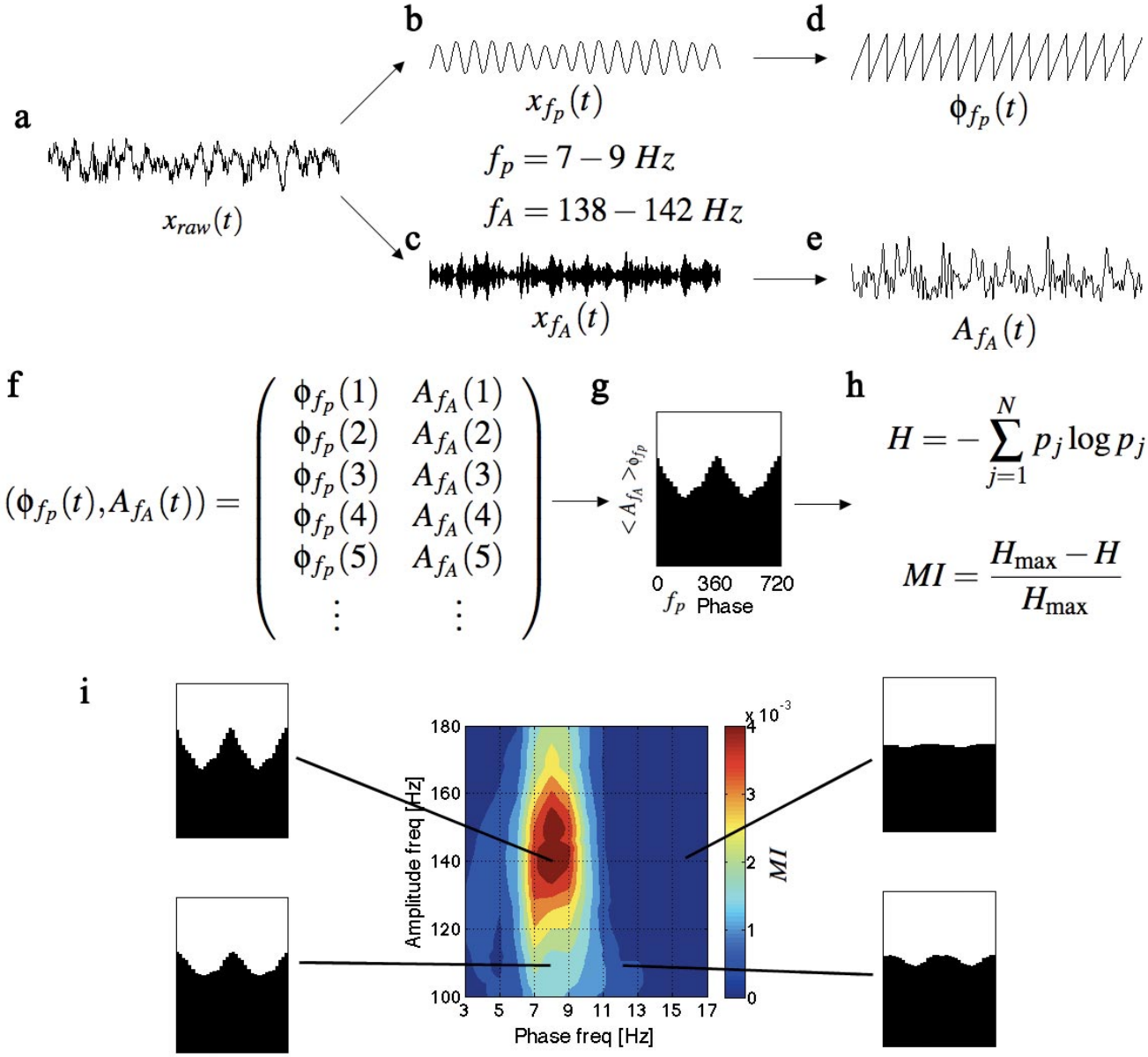

Fig. S2. Steps in the computation of the modulation index (MI) and of the comodulogram plot (see *Data Analysis* in SI Text). (*a*–*c*) The raw signal (*a*) is filtered at the phase (*b*) and amplitude (*c*) frequency ranges of interest. (*d* and *e*) Next, the phase (*d*) and the amplitude (*e*) time series are calculated from the filtered signals by using the Hilbert transform. (*f* and *g*) A composite time series (*f*) is then constructed and used to obtain the mean amplitude values at each 20° phase bin (*g*) (2 cycles shown for clarity). (*h*) The MI is finally obtained by applying a normalized entropy measure to the mean amplitude vector. (*i*) The comodulogram plot is constructed by representing in pseudocolor scale the MI values of multiple phase–amplitude frequency pairs.

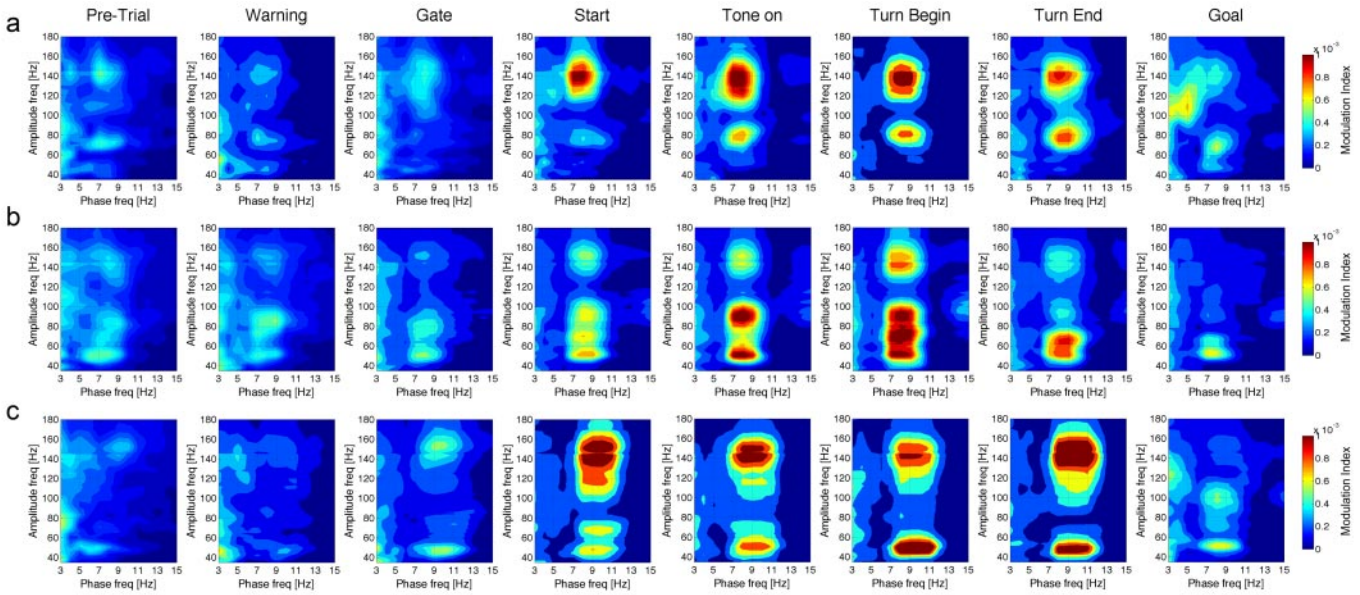

Fig. S3. Cross-frequency couplings can occur at LG, HG, or in the whole gamma range simultaneously. Rows (*a*–*c*) show the phase-to-amplitude comodulograms (obtained at the distinct task events) of 3 additional rats. In *a*, theta phase amplitude modulation occurred more in the HG band than in the LG band; in *b*, the entire gamma band was modulated by the theta phase; and in *c*, modulation appeared more in the LG band. Notice further that *b* constitutes an example of a tetrode that presented much higher modulation at the gamma range than at the HFO range. For each rat, the results were obtained from 1 representative tetrode located at the superficial layers of the dorsal CA1 region averaged over sessions (*a* and *c*: 5 sessions; *b*: 10 sessions).

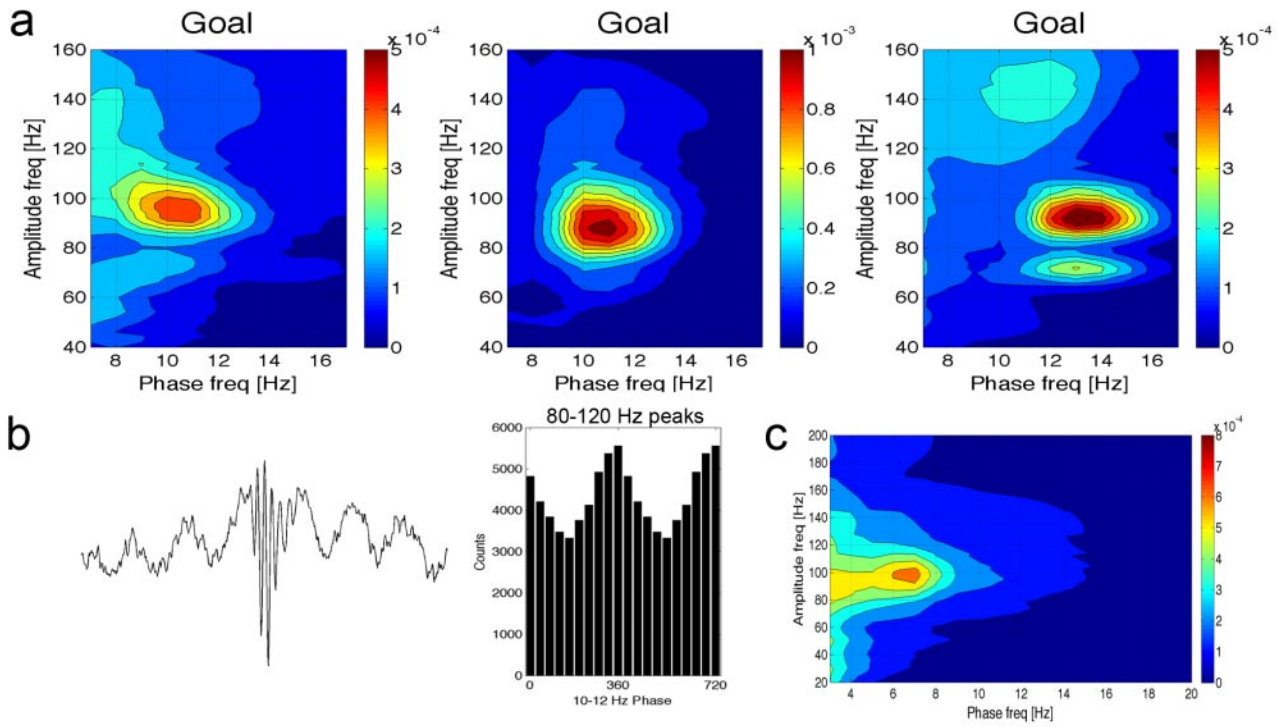

Fig. S4. The amplitude of the 80- to 120-Hz band is modulated by a ''high'' theta oscillation in the striatum during the task goal. (*a*) Phase-to-amplitude comodulograms of 3 distinct animals. These 3 rats presented an amplitude modulation of the 80- to 120-Hz frequency band by a high theta frequency during the goal period. Note, however, that their peak phase modulation frequency differed. (*b*) Averaged raw signal (600 ms shown) during the goal event obtained by centering the signal at the peaks of the 80- to 120-Hz oscillation (*Left*; see *SI Text*) and the phase histogram of the 80- to 120-Hz oscillation peaks (*Right*). Note that the high theta oscillation can be seen in the averaged raw data and that the 80- to 120-Hz oscillation peaks at the trough of this oscillation. (*c*) Phase-to-amplitude comodulogram averaged over all task events. Because the modulation by the high theta occurred only during the final period of the task, this effect cannot be noticeable in this procedure. Note further that the 80- to 120-Hz amplitude modulation by the ''low'' theta oscillation is prominent in such analysis. *a* was obtained by averaging the results of all striatal tetrodes and sessions (for each rat); *b* was obtained by averaging all striatal tetrodes during 1 session of the animal shown at the middle of *a*; *c* was obtained by averaging the results of all 3 animals.

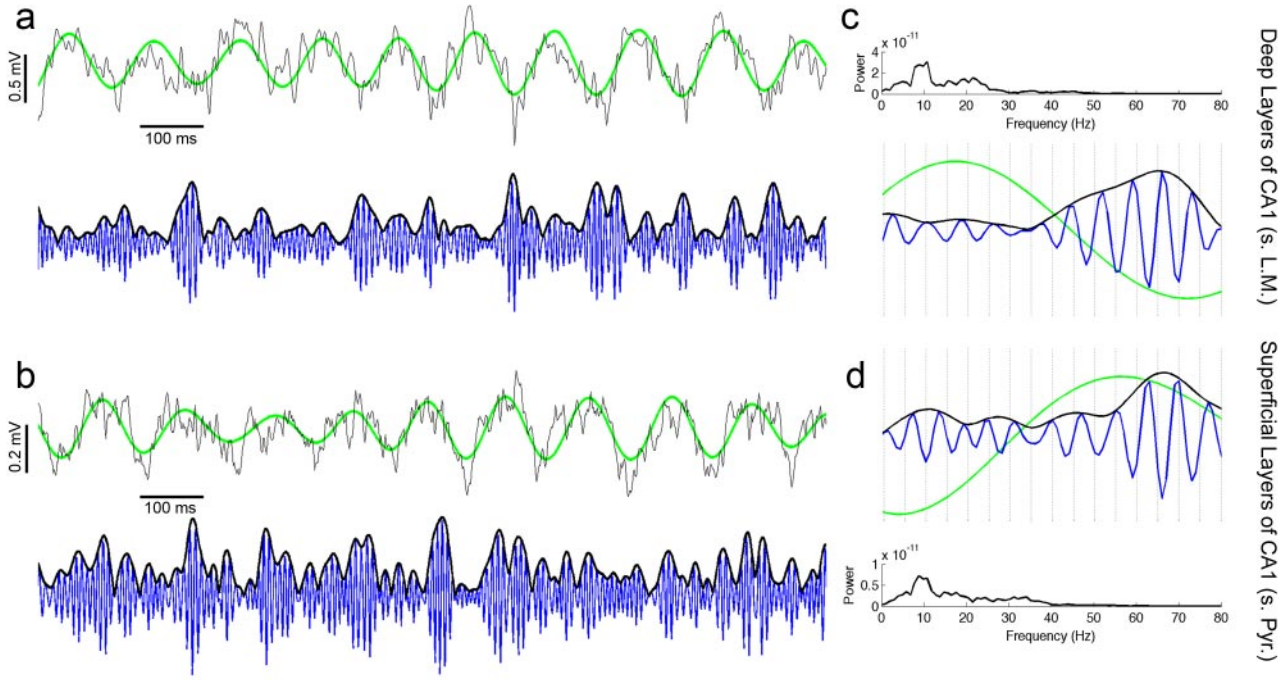

Fig. S5. The theta phase of peak HFO amplitude reverses between superficial and deep CA1 layers. (*a*) Representative hippocampal LFP trace and filtered signals during a single trial. Raw trace (thin black line) and the theta (7–12 Hz) filtered signal (thick green line) obtained from 1 tetrode located at the deep layers of the CA1 region are shown at the top (1 s shown). The (amplified) HFO (120–160 Hz) filtered signal is shown at the bottom (thin blue line). The thick black line represents the HFO amplitude envelope. (*b*) Same as in *a* but for a tetrode located at the superficial layers of the CA1 recorded simultaneously. (*c* and *d*) Power spectrum (in V^2/Hz) of the HFO amplitude envelope and an expanded view of the filtered signals [100 ms shown (corresponding to the horizontal bars in *a* and *b*)]. Note the phase reversal of both theta (green) and HFO (blue) signals between the superficial and deep CA1 layers. Notice further that the theta peak in the amplitude envelope power spectrum constitutes yet another independent analysis demonstrating the modulation of HFO by the theta rhythm.

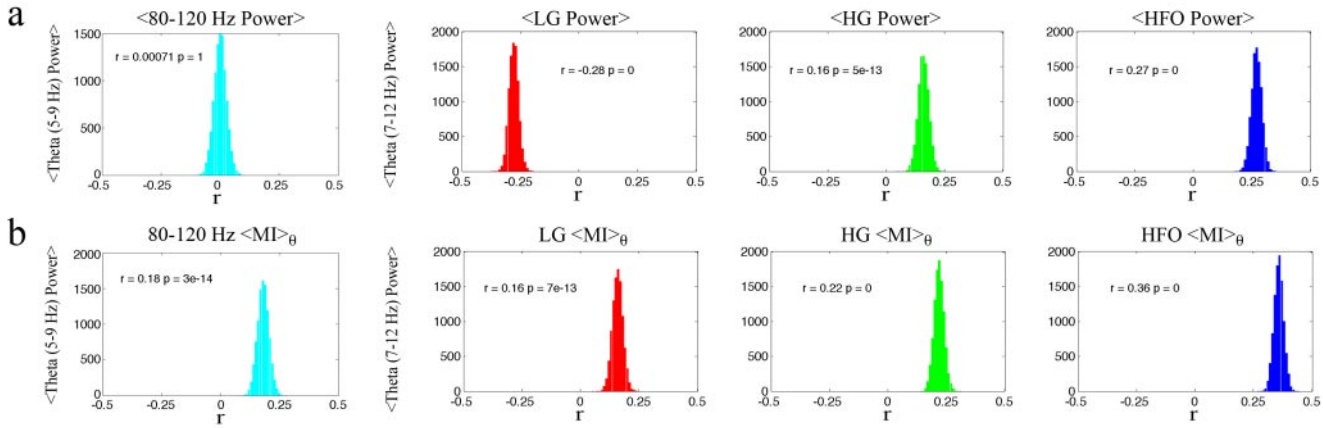

Fig. S6. Theta power correlates with the power of fast oscillations and cross-frequency coupling strength. (*a*) Bootstrap analysis (10,000 replicates) applied to the correlation coefficient (*r*) between theta power and the power of the fast oscillations. Theta power is not correlated with the 80- to 120-Hz oscillation power in the striatum (cyan). In the hippocampus, theta power is negatively correlated with LG power (red), whereas it is positively correlated with both HG (green) and HFO (blue) powers. (*b*) Bootstrap analyses of the correlation coefficient between theta power and the averaged modulation index ($\langle MI \rangle_\theta$) values of striatal and hippocampal fast oscillations, showing that theta power is positively correlated with the intensity of phase-to-amplitude modulation of all higher-frequency rhythms studied. Results were obtained from the pooled data of all tetrodes, sessions, and animals (striatum: $n = 303$; hippocampus: $n = 360$). Both the mean power values and $\langle MI \rangle_\theta$ were normalized to permit combined analyses of distinct tetrodes and animals (see *SI Text*).

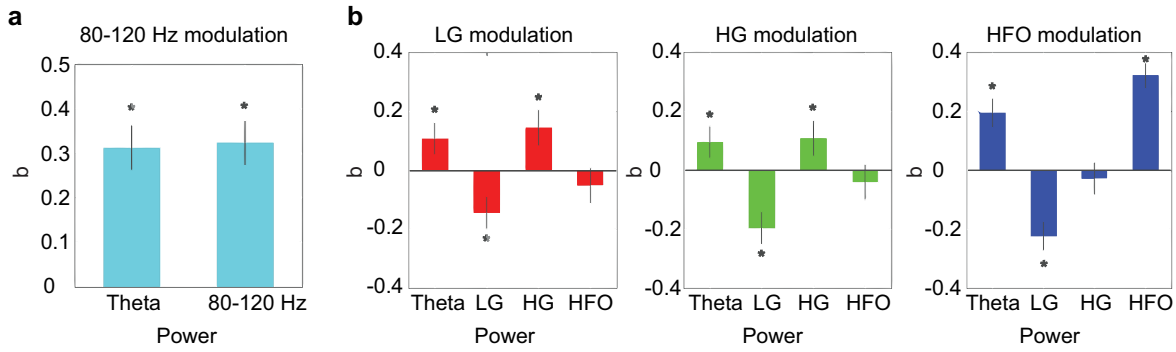

Fig. S7. Cross-frequency couplings depend on the power of multiple frequency bands. Plots show standardized regression coefficients obtained from multiple regression analyses between the intensity of the amplitude to theta phase modulation (dependent variable) and the mean power of frequency bands of interest (independent variables). (*a*) Regression analysis of striatal LFP recordings, showing that the modulation of 80- to 120-Hz oscillations depend equally on their own power and on the power of cooccurring theta rhythms. (*b*) Regression analysis for 3 high-frequency oscillations in the hippocampus. Notice that the theta modulation of HG and HFO are mutually independent. These results were obtained from the pooled data of all tetrodes, sessions, and animals (striatum: $n = 303$; hippocampus: $n = 360$). The vertical black lines represent the 99% confidence intervals. *, statistically significant coefficients ($P < 0.00001$). The intensity of theta phase modulation was assessed by computing the mean modulation index values at the theta band (see *SI Text*).

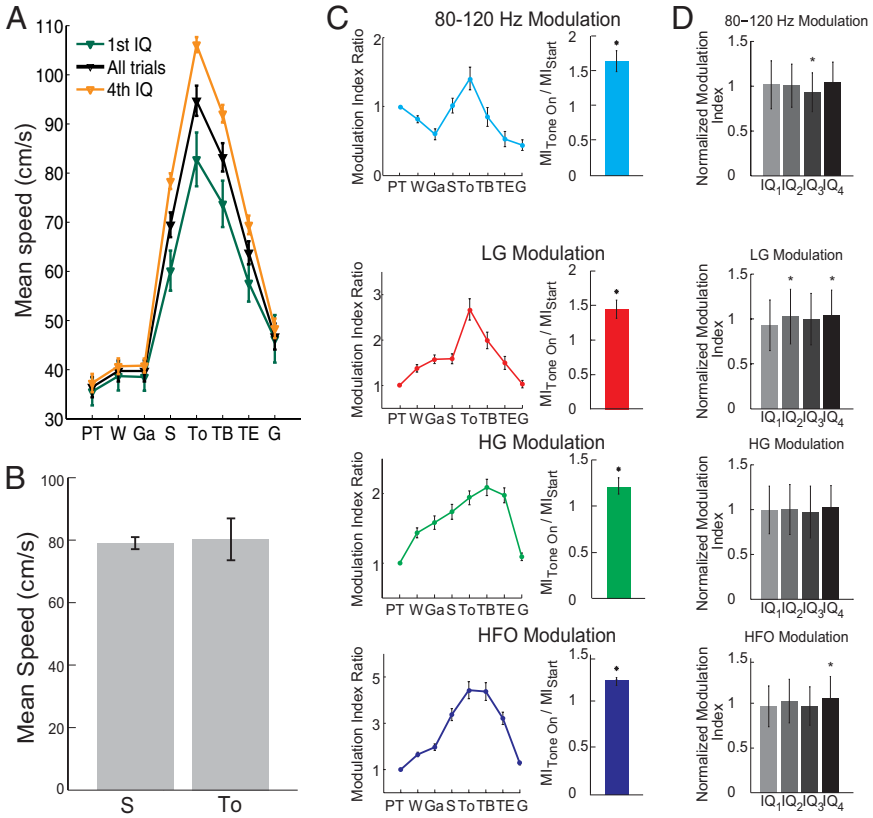

Fig. S8. Running speed does not account for the different intensities of cross-frequency phase-amplitude couplings during different task epochs. (*A*) Mean speed as a function of the task event for the animal shown in Fig. 2. The black trace shows the mean speed over all trials and sessions. The orange and the green traces show the mean speed for the fastest and the slowest quartile trials, respectively. Error bars represent SEM. (*B*) Mean speeds of subset of trials for this animal chosen to equate the running speed for the ''Tone Onset'' and ''Start'' task events (i.e., the fastest trials for the Start event and the slowest trials for the Tone Onset event were chosen). These trials were used for the analysis in *C*. (*C*) (*Left*) Mean modulation index (MI) values for striatal 80–120 Hz (top row) and hippocampal high-frequency rhythms (bottom 3 rows, as labeled), expressed as a ratio of the pre-trial MI value, as a function of the task event for all trials and sessions for the same animal as in *A*. (*Right*) Mean MI ratio between the Tone Onset and Start events computed over the speed-controlled trial subsets from *B*. *, statistically significant difference from 1 ($P < 0.05$, paired *t* test). (*D*) Normalized MI versus speed computed for each speed interquartile (IQ1 to IQ4: slowest to fastest) and averaged over all rats, tetrodes, and sessions (see *SI Text*). Note the absence of meaningful differences in MI values across the quartiles; in particular, notice that the MI values are not increasing across the quartiles. Bars represent SD. *, $P < 0.05$ (Friedman test).

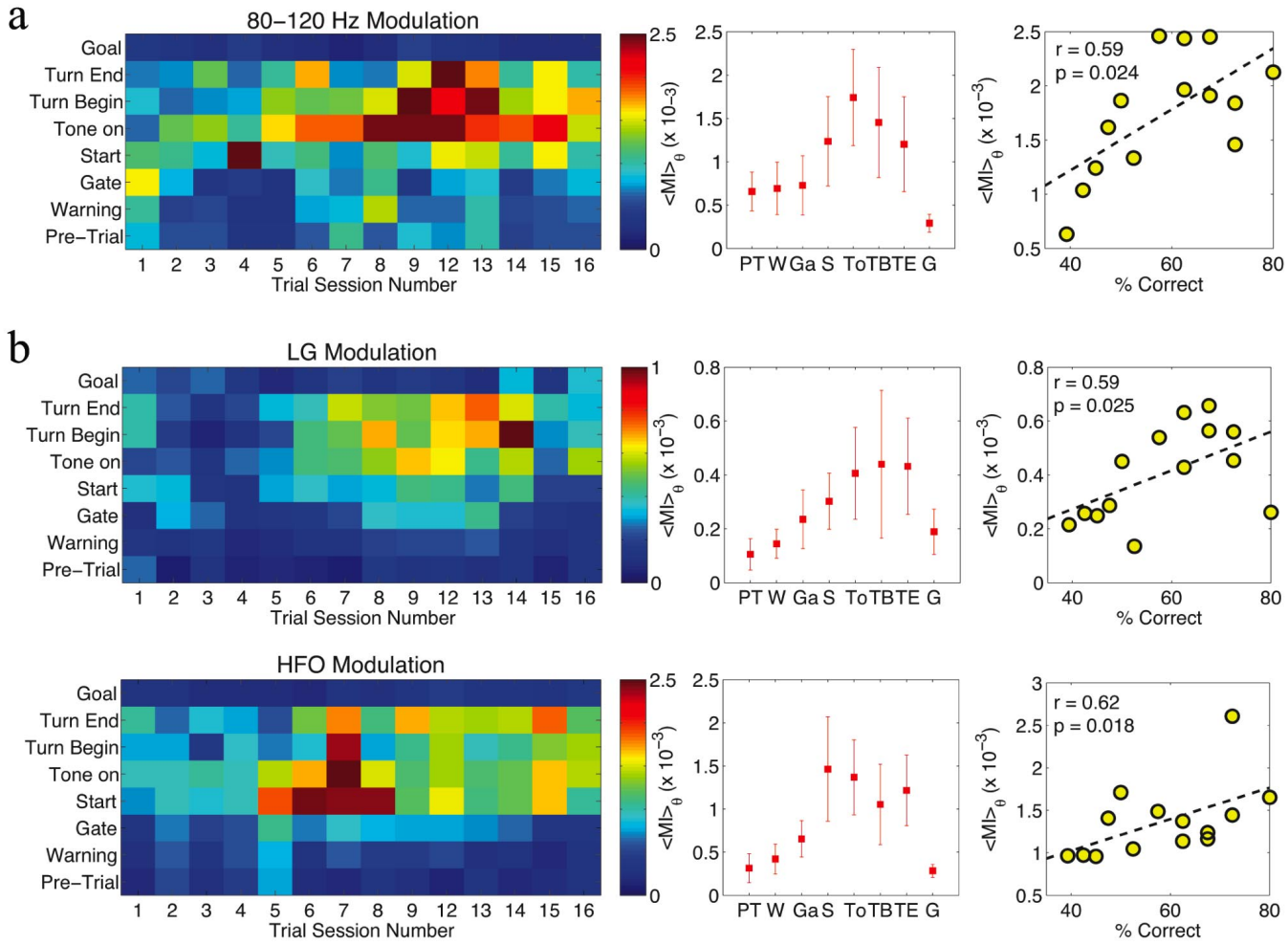

Fig. S9. Intensity of amplitude modulation may correlate with learning. (*a*) (*Left*) Pseudocolor plot showing average modulation index ($\langle MI \rangle_\theta$) values as a function of task event and session number for striatal 80–120 Hz modulated by theta. (*Center*) The mean $\langle MI \rangle_\theta$ values as a function of the trial event obtained by averaging $\langle MI \rangle_\theta$ over all sessions. Error bars represent SEM. (*Right*) Correlation between $\langle MI \rangle_\theta$ during the Tone Onset event and percent correct performance. (*b*) (*Left*) $\langle MI \rangle_\theta$ as a function of task event and session number for hippocampal LG (upper plot) and HFO (lower plot) modulated by theta. (*Center*) Mean hippocampal $\langle MI \rangle_\theta$ versus task event for LG (*Upper*) and HFO (*Lower*) averaged over all sessions. (*Right*) Correlation between $\langle MI \rangle_\theta$ and percent correct for hippocampal LG and HFO. Results in *A* and *B* were obtained from 1 tetrode in the striatum and in the superficial layers of CA1, respectively, that did not move their positions during the sessions analyzed. We could not, however, consistently study the correlation of the modulation index with learning because most of the tetrodes moved their position across the sessions (e.g., from deep to superficial CA1 layers) and also because some animals were subjected to distinct number of trials in different experimental session days. Both factors make unreliable a direct comparison of the modulation index across distinct experimental sessions (for instance, the intensity of the modulation depends on the theta power (Figs. S6 and S7) and theta power is known higher in the striatum lacunosum-moleculare (corresponding to deep layers recordings) than in striatum pyramidale (superficial layers recordings); note the change in the *y*-scale between Fig. S5 *a* and *b*).